Annales Geophysicae (2004) 22: 3461–3478
SRef-ID: 1432-0576/ag/2004-22-3461
© European Geosciences Union 2004

Annales Geophysicae

Imaging riometer observations of drifting absorption patches in the morning sector

R. A. Makarevitch[1], **F. Honary**[1], **I. W. McCrea**[2], **and V. S. C. Howells**[2]

[1]Department of Communication Systems, Lancaster University, Lancaster, LA1 4YR, UK
[2]Rutherford Appleton Laboratory, Chilton, Didcot, OX11 0QX, UK

Received: 10 December 2003 – Revised: 30 June 2004 – Accepted: 2 July 2004 – Published: 3 November 2004

Abstract. Observations by a 7×7-beam imaging riometer in Kilpisjärvi, Finland (∼66° MLAT) of the drifting cosmic noise absorption (CNA) structures in the morning sector near the zonal drift reversals are presented. The examination of the absorption intensity images revealed several regions with enhanced CNA (absorption patches) slowly drifting through the riometer field of view (FoV). The absorption patches were found to vary in shape, orientation (for elongated arc-like patches), and drift direction. The latter was calculated from the regression lines to positions of the absorption maxima in the FoV images and compared with the direction of electrojet plasma flow from horizontal magnetic perturbations and (for one event) tristatic ion drift velocities in the F-region. A reasonable agreement was found between these directions both in point-by-point comparisons and in terms of direction reversal timings. The absorption patches of lower intensity appear to have smaller drift velocities and to be associated with weaker magnetic perturbations. These results are consistent with the notion that relatively slow motions of the auroral absorption near the zonal drift reversals are associated with the $\boldsymbol{E}\times\boldsymbol{B}$ drift of the entire magnetic flux tube as opposed to the gradient-curvature drift of energetic electrons injected into the ionosphere at the substorm onset. The absorption drift velocity magnitude, on the other hand, was found to be substantially lower than that of the plasma flow based on the results of limited comparison with tristatic ion drift measurements. A comparison of the drift directions with those of the patch elongation showed that a considerable number of patches had these directions close to each other. Using this observation, we demonstrate a satisfactory agreement between the patch drift velocities (both in direction and magnitude) as determined from the absorption images and keograms under the assumption that some patches were propagating in a direction that was significantly different from the perpendicularity to elongation.

Key words. Ionosphere (auroral ionosphere; electric fields and currents; plasma convection)

Correspondence to: R. A. Makarevitch
(r. makarevitch@lancaster.ac.uk)

1 Introduction

The spatial resolution of riometer systems has been gradually increasing over the years of research from several hundred (widebeam riometer sets) to a few tens of kilometers (imaging riometers), which has significantly extended the range of detectable absorption structures and enabled more accurate determination of the cosmic noise absorption (CNA) drift velocity (e.g. Hargreaves, 1970; Berkey et al., 1974; Nielsen, 1980; Kikuchi et al., 1990; Stauning et al., 1995; Kainuma et al., 2001; del Pozo et al., 2002, and references therein).

Berkey et al. (1974), by considering a large number of synoptic absorption maps from over 40 riometer stations in the subauroral, auroral, and polar cap latitudes during substorm conditions, concluded that the absorption maxima in most cases moved eastward from the substorm injection area with a velocity of 0.7–7 km/s, consistent with the idea that the motion of auroral particles injected during the substorm into the nightside ionosphere is governed by gradient-curvature (GC) drift. Hargreaves (1970), using the absorption data from 4 closely-spaced riometers, found a significantly lower (from 80 m/s to 3.3 km/s) range of velocities of eastward expansion with a significant number of absorption events expanding westward. This casted doubt on the validity of a simple injection-drift model and suggested that another mechanism could be responsible for the observed drifts of absorption features. Hargreaves (1970) proposed that the precipitating electrons are moving together with the entire magnetic flux tube and hence their motion is governed by the $\boldsymbol{E}\times\boldsymbol{B}$ drift or, in other words, by the high-latitude convection.

Later Nielsen (1980) in a four-narrow-beam riometer experiment in Northern Scandinavia studied the dynamics of absorption spikes during the substorm expansion phase and discovered that the spike velocity appeared to be different from the $\boldsymbol{E}\times\boldsymbol{B}$ drift velocity. Moreover, a comparison with the STARE radar measurements showed an almost ideal coincidence over the observed range from 0.3 to 3.0 km/s between the spike velocity and the velocity of the STARE backscatter poleward border.

More recently, Kikuchi and Yamagishi (1990) and Kikuchi et al. (1990), by employing the data from the scanning narrow beam riometer at the Syowa Antarctic station, showed that the drift pattern of the elongated arc-like regions with enhanced absorption was similar to that of the ionospheric convection, thus extending the result of Hargreaves (1970) towards the smaller scales (30–60 km versus ∼250 km in Hargreaves, 1970). Using the imaging riometer in Søndre Strømfjord, Greenland and nearby magnetometers, Stauning et al. (1995) investigated the dayside convection disturbances accompanied by the CNA enhancements and demonstrated that the disturbances propagate poleward from the cusp latitudes across the polar cap with velocities of 0.4–0.9 km/s. Kainuma et al. (2001) gathered significant data statistics on the velocity of auroral arc-like absorption regions from the imaging riometer in Poker Flat, Alaska with a beam separation of 10–20 km. These authors concluded that the narrow absorption regions appeared to move with a velocity that was consistent with the $\boldsymbol{E}\times\boldsymbol{B}$ drift. A similar conclusion was also reached in several case studies that used the data from the Imaging Riometer for Ionospheric Studies (IRIS) in Kilpisjärvi, Finland (Nielsen and Honary, 2000; Kavanagh et al., 2002; del Pozo et al., 2002). In the latter study, however, it was demonstrated that this conclusion seemed to hold only for relatively stable auroral arcs and that during the substorm expansion phase the absorption drift velocity was significantly different from that of convection, as observed by the European Incoherent Scatter (EISCAT) radar facility, a result similar to that of Nielsen (1980).

In most of the above studies, including those that concentrated on the drift patterns of arc-like absorption structures utilizing large data statistics (Kikuchi et al., 1990; Kainuma et al., 2001), the drift velocity was calculated under the assumption that the arc-like structures propagate in a direction perpendicular to that of elongation, which reflects the difficulty of determination of the velocity component along the arc. Therefore, to complement previous studies and to test the validity of this assumption we decided to exploit the imaging capability of the IRIS facility by using the absorption field of view (FoV) images and in addition to the drift velocity, to examine the shape of absorption patches. We developed a simple method of absorption patch identification based on the absorption images that does not require manual sifting through the data. In order to conclude on the mechanisms governing the drift of auroral absorption patches, in this study we concentrate on 10 events in the morning sector featuring a change in patch zonal velocity from eastward to westward, thus exploring the absorption drifts in this transitional region.

2 Observations

The IRIS facility in Kilpisjärvi, Finland (69.1°N, 20.8° E, ∼66° MLAT) became operational in September 1994. It records the cosmic noise absorption at 38.2 MHz in 49 different directions with 1-s resolution, although some post-integration is usually employed to increase the signal-to-noise ratio (Browne et al., 1995). The bulk of CNA is due to precipitating auroral electrons with the energies above 25 keV that ionize the neutral atmosphere at D-region altitudes below 95 km (del Pozo et al., 1997). IRIS is therefore capable of providing a continuous picture of the particle precipitation with good temporal resolution in 49 directions centered around the zenith beam. To facilitate the riometer data handling it is customary to combine the data from all 49 directions in one absorption intensity FoV image using a grid in geographical coordinates and interpolating the data. The absorption keograms obtained by fixing the geographic longitude or latitude provide a simple method of visualising the data. For more detailed analysis, however, the examination of the image series is preferable. More details on the imaging riometer technique and methods of data processing can be found in Detrick and Rosenberg (1990).

To put the motion of absorption features in the context of the ionospheric currents in this study we used the magnetic field data from the Kilpisjärvi (KIL) fluxgate magnetometer of the International Monitor for Auroral Geomagnetic Effects (IMAGE) network (e.g. Lühr et al., 1998) co-located with the IRIS facility. The IMAGE magnetometers measure the north (X), east (Y), and vertical (Z) components of magnetic field with 10-s resolution, from which the picture of electrojet currents at E-region heights of 100–110 km can be estimated.

As mentioned, in this study we decided to look at the periods in the morning sector of IRIS observations when the absorption structures changed drift direction from eastward to westward. In total, 10 events with 10 such reversals, as seen from the east-west keograms, were selected for the analysis, the criterion being that the event should show absorption structures first propagating eastward and then westward. Table 1 shows the complete list of events; all times shown are in UT; MLT≅UT+2.7. In addition to event start and end time, Table 1 shows K_p indices (for the duration of event), IMF B_y and B_z GSM components in nT (typical for event) as measured by the ACE magnetic field instrument (Smith et al., 1998), sunrise time, and drift reversal times from absorption keograms. Note also that during event 2 two reversals were seen, first at ∼06:33 UT (from east- to westward) and the opposite at ∼08:00 UT. The magnetic activity was from weakly to moderately disturbed, whereas IMF conditions varied from event to event. In the following section the riometer and magnetometer data from 14 February 2001 are presented and discussed as a representative example of events.

For this event the data on the ionospheric density, electron and ion temperatures, and ion drift velocities from the EISCAT facility were also available. The EISCAT UHF tristatic incoherent radar system (∼928 MHz) consists of three parabolic dish antennas with one site in Tromsø combining both transmitting and receiving capabilities, and two remote site receivers at Kiruna and Sodankylä (Rishbeth and Williams, 1985). On 14 February 2001 EISCAT operated in a CP-1 common mode with the Tromsø radar looking along

Table 1. Selected periods of the IRIS observations.

Event	Date	Start Time	End Time	K_p	B_y	B_z	Sunrise	Reversal Time
1	24 October 1994	01:00	11:00	4 5 5−4−	na	na	06:28	06:35
2	4 November 1994	03:00	09:00	5+3+	na	na	07:19	06:33
								08:00
3	12 March 1995	01:00	09:00	6 6 4	−5	0	05:24	05:39
4	10 April 1995	05:00	10:00	5−4 5−	−4	−4	05:00	07:54
5	08 September 1995	04:00	12:00	5+6+5+	5	−4	04:00	07:09
6	18 September 1997	04:00	10:00	5 3+2+	−10	−8	04:08	07:20
7	30 August 1998	03:00	09:00	4−2+	4	−3	03:00	07:00
8	30 September 1999	04:00	09:00	5+4	4	−5	04:53	07:07
9	14 February 2001	04:00	09:00	4−3−	−3	−4	07:21	07:22
10	25 December 2002	02:00	05:00	3 3−	5	4	04:59	03:40

the magnetic field line at an azimuth of 183.8° and elevation of 77.1° and receiver beams in Kiruna and Sodankylä intersecting the Tromsø beam at an altitude of 293 km. We present the EISCAT measurements and derived ionospheric parameters in Sect. 5.

3 Event on 14 February 2001

Figure 1 shows the IRIS absorption intensity images from 14 February 2001, 04:00–09:00 UT, in 1-min resolution (to make the diagram readable only every other image is shown). For each 1-min frame, the black dot indicates the absorption maximum position inside the IRIS FoV. To obtain a smoother variation of the absorption maximum position, a parabolic function was fitted to the point of maximum and two immediate neighbors in the grid (both along x and y axes) and the point of parabola maximum was taken as the absorption maximum position. In addition to the black dot marking the current fitted maximum position, up to four previous fitted maximum positions are indicated in Fig. 1 by grey dots, the lightest being the absorption maximum of 4 min before the current one. The coloured lines in each frame mark the half-power contours (absorption maximum minus minimum in the FoV). The colour of the line is the same for each individual patch.

We defined the start and the end frames for each absorption patch as follows. We first considered if the maximum position changed from one 1-min frame to another by more than 100 km (approximately 1/2 of the FoV dimensions). This limitation implies the largest drift velocity of 1667 m/s to be measured by tracing the absorption maximum, which is sufficient for events of interest with the observed velocities in the vicinity of drift reversals. If the jump in the absorption maximum position was more than 100 km (we marked such frames in Fig. 1 by a big yellow letter J in the top left corner of the frame), the frame count for a patch was reset. The minimum "duration of a patch" (between jumps in maximum) was taken to be 4 min (two frames in Fig. 1). The maximum duration of the patch was limited by 20 min. We marked in Fig. 1 the start and the end frame for each individual patch by letters B and E, respectively. Thus the start frame for patch 06 in Fig. 1 (the patch number is indicated in the right bottom corner) coincides with the jump at 05:32 UT and the end frame is at 05:52 UT, 1 min before the next jump at 05:53 UT (the frame is skipped). One should note here that by restricting the maximum number of frames we artificially increased the number of patches and that some successive patches are in fact the same patch (as, for example, patches 07–10). However, in this way we are certain that our patch velocity calculations (see below) refer to reasonably small periods of time, so that the average velocity (for each individual patch) represents well the sense of the patch motion. The latter is illustrated in Fig. 1 by the previous successive positions of the absorption intensity maximum (we marked the previous positions only for the same patch). Thus, it is clear from Fig. 1 that, for example, patch 05 (green contour) was drifting eastward. To emphasize this feature we indicated the average direction of the patch motion (for each individual patch) in each frame of Fig. 1 by a blue straight line with the origin in the absorption maximum (black dot). The motion of the absorption maximum was not always simple and steady, that is along the average direction of drift, for example, as for patch 15 (blue contour) for which the maximum first (08:06–08:08 UT) migrated eastward and then (08:10–08:20 UT) drifted westward. We return to this issue in Sect. 4 where we quantify the uncertainty in the patch drift velocity determination and restrict the database used for further analysis.

Another feature illustrated in Fig. 1 is the shape of the absorption patch and its relationship with the patch drift velocity. One can see in Fig. 1 a great variability in the patch shapes and directions of the longest dimension (for elongated patches), even within relatively short periods of time. For example, patch 00 (blue) was elongated in the east-west direction while successive patches 01 (yellow) and 02 (green) were more diagonally-elongated. Patch 04 (yellow), on the other hand, is clearly rotated by ∼90° with respect to patch 02. To quantify the size, shape, and orientation of the

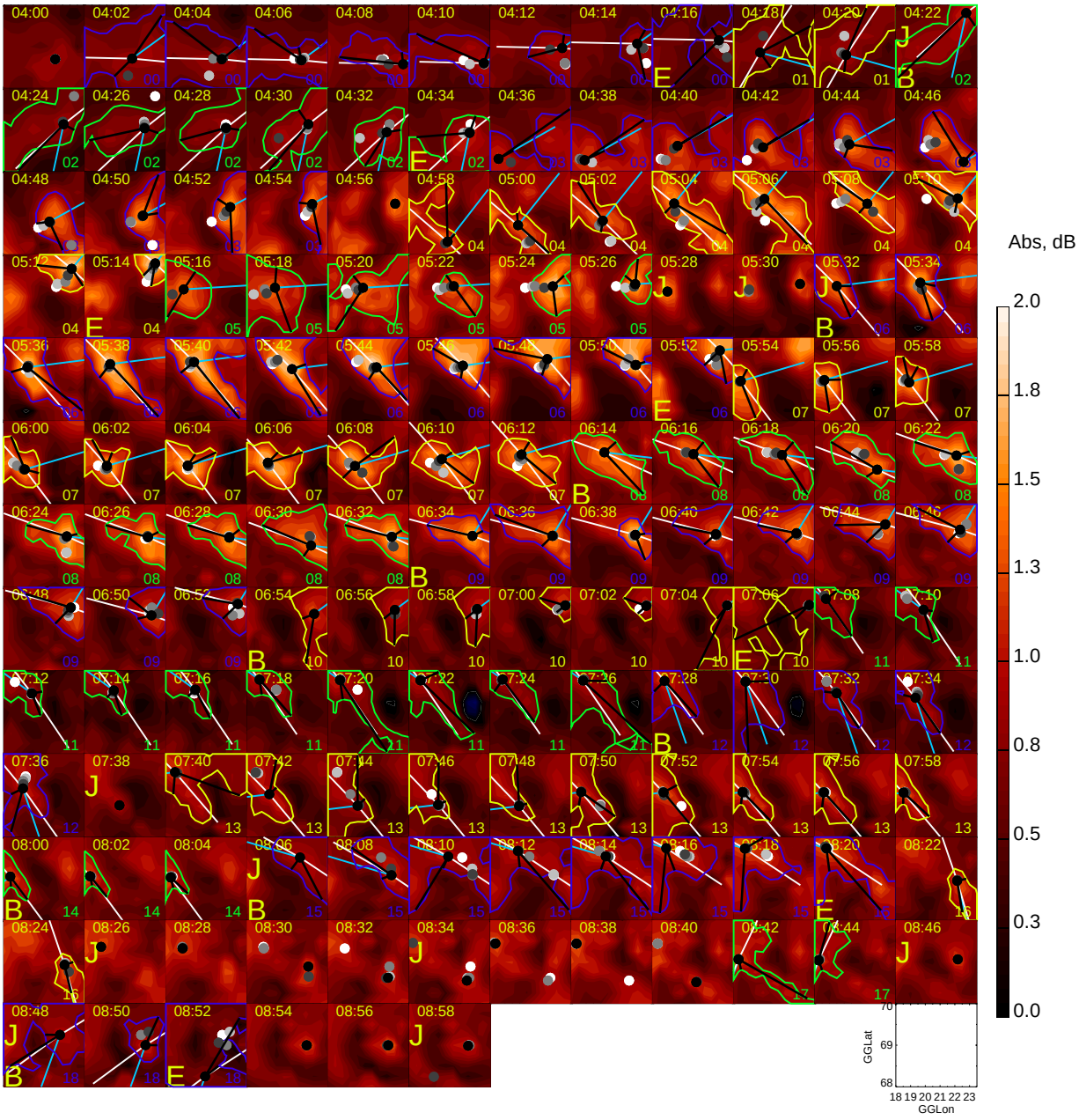

Fig. 1. Sequence of the IRIS absorption intensity images at 1-min resolution for 14 February 2001, 04:00–09:00 UT. The scale for the absorption is indicated on the right. For each frame the absorption maximum position is shown by the large black dot. Coloured contours represent the half-power contours for each individual patch with the patch number indicated in the right bottom corner of each image. The four previous absorption maximum positions (for the same patch) are shown by grey dots, with the lightest dot being the maximum position 4 min before the current one. The yellow letter J indicates whether a jump of more than 100 km has occurred in the absorption maximum location, and letters B and E indicate the start and the end frame of the individual patch, respectively. The short (long) straight black line with the origin in the black dot shows the shortest (longest) distance between the absorption maximum and the half-power contour. The white straight line indicates the average direction (for individual patches) of the patch's longest dimension in cases when the standard deviation in this direction was less than 40°. The blue straight line shows the average motion direction (for each individual patch).

absorption patch we introduced the following two estimates. Two black straight lines with the origin in the absorption maximum in Fig. 1 show the longest and shortest distance between the absorption maximum and half-power contour (excluding the points at FoV borders). Although quite variable even for each individual patch, these estimates provide a useful framework for studying the relationship between the absorption patch orientation and drift direction. Figure 1 shows by white straight lines the direction of the patch's longest dimension obtained by averaging these directions for all frames

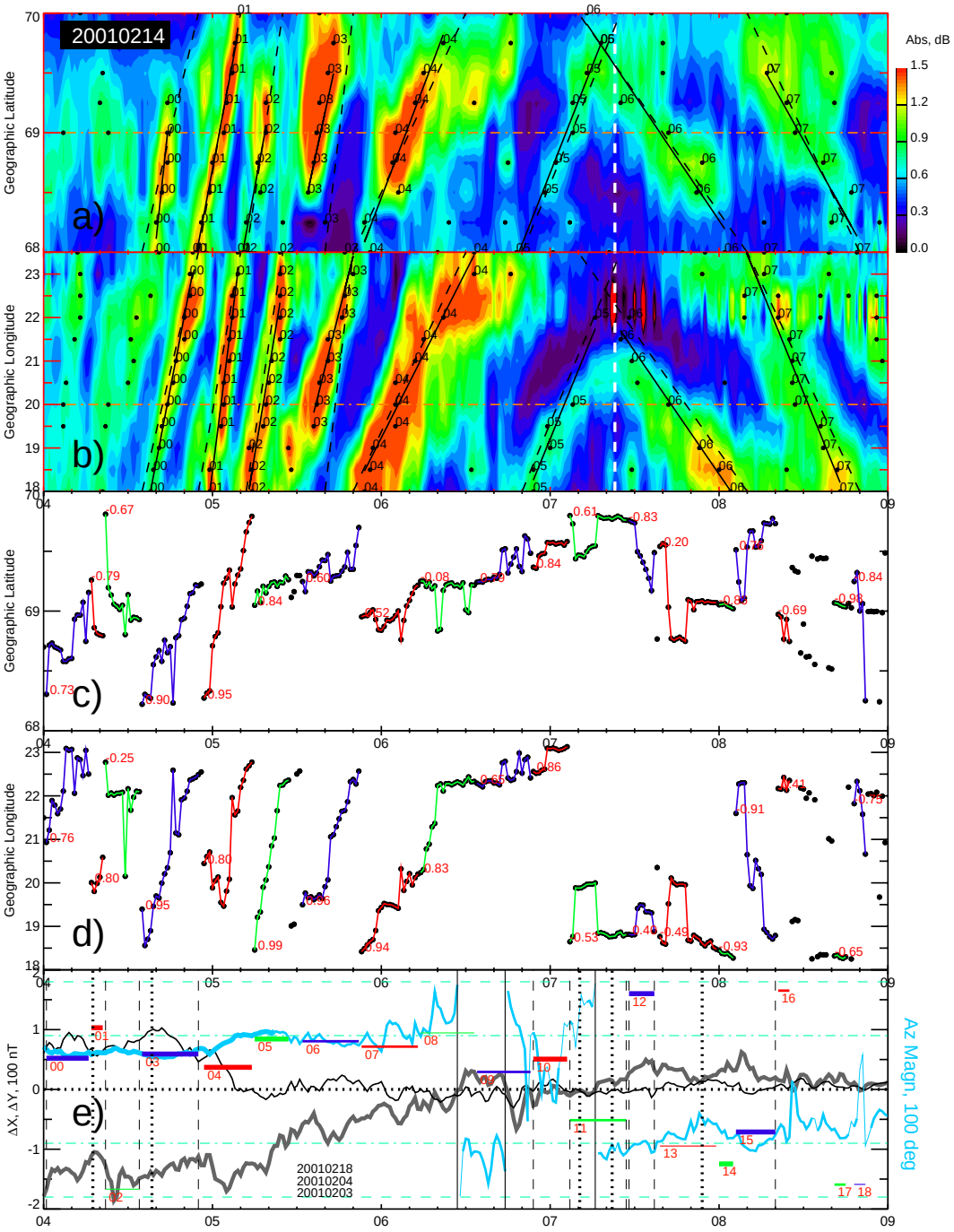

Fig. 2. The IRIS absorption keograms for 14 February 2001, 04:00–09:00 UT, at 1-min resolution for **(a)** 20° E and **(b)** 69° N. The keogram geographic longitude and latitude are indicated in (b) and (a), respectively, by the dash-dotted orange lines. The scale for the absorption is indicated on the right of panel (a). The black dots show the local maxima in time for the absorption. The dashed black lines represent the initial guesses for the absorption patch movements, while the solid lines denote the best fits to all maxima located within 10 min of the initial guesses. The maxima for each patch are marked by digits showing the patch number (from 00 to 07). The vertical dashed white line shows the reversal time of the patch motion direction (from eastward to westward). Panels **(c)** and **(d)** show the location of the absorption maxima identified in Fig. 1 within the IRIS field of view. The maxima for each individual absorption patch are connected by the coloured lines with the correlation coefficients for each patch shown by red digits nearby. Panel **(e)** shows the ΔX (ΔY) component of magnetic perturbations from KIL station at 1-min resolution by the heavy (light) black line. The days used for QDC calculations are indicated at the bottom of panel (e). The blue line represents the azimuth of electrojet plasma flow as inferred from the magnetometer data. The thickness of the line corresponds to the magnitude of horizontal perturbations. The solid vertical lines denote the reversals in azimuth sign. Also shown in panel (e) by coloured horizontal lines are the azimuths of the absorption patch motion. The patch number from Fig. 1 is shown at the bottom of each line.

in a patch (longer black lines) if the standard deviation was less than 40° (to increase the data statistics, for this averaging we allowed up to 3 frames with the largest deviation to be discarded). One can notice that this restricted estimate represents reasonably well the sense of the patch orientation (see, for example, patches 00, 08, 12). The angle between the patch drift velocity vector and the direction of the longest dimension (blue and white straight lines, respectively) greatly varies from patch to patch; if patch 04 drifts in the direction that is more or less perpendicular to the patch elongation direction, for patch 15 this angle is closer to zero than to 90°.

With respect to the variation of the patch average drift direction (indicated in Fig. 1 by the blue line) with time, one can see that during (roughly) the first half of the event (from 04:00 to 06:30 UT) the absorption patches were drifting predominantly eastward (with exception of patch 02). The first patch to drift westward after that was patch 11 (green) from 07:08 to 07:26 UT. The next patch 12 drifted slightly eastward, but the next two long-duration patches (13 and 15) clearly drifted westward. To explore the time variation in more detail we present the next diagram, Fig. 2, which shows the same data as Fig. 1 but in a different format. Panels (a) and (b) are the absorption keograms at 20° E (east of geographic north) and 69° N, respectively. This geographic longitude and latitude are indicated in panels (b) and (a), respectively, by the dash-dotted horizontal lines. One can immediately notice in Figs. 2a–b several absorption patches propagating first, from 04:00 to ∼07:30 UT, eastward and northward and then, after 07:30 UT, westward and southward. The patch near 07:30 UT actually changed its drift direction while being inside the IRIS FoV, so that the east-west keogram (b) clearly shows the drift direction reversal at ∼07:22 UT and we marked this time by the white dashed vertical line. Since this patch hardly reaches the central longitude of the FoV (20.75° E), for the north-south keogram (a) we selected a slightly more westward location to make the reversal at 07:22 UT clearer.

The existence of the clearly defined patches in the absorption keograms allows one to estimate the patch velocity, for example, using the method described in some detail in Kainuma et al. (2001), that is by fitting a straight line to the absorption maxima for each patch. We first found all local absorption maxima in time for each of the latitudes and longitudes in panels (a) and (b), respectively. To restrict the number of such maxima the minimum period of time between maxima was set to 10 min and the minimum height of the maximum (with respect to adjacent minima in time) was set to 0.1 dB. The obtained maxima are shown in Figs. 2a–b by black dots. We then assigned to each patch a start and end time; these times are connected in Figs. 2a–b by dashed black lines which thus represent the initial guesses for the regression lines. For the following least-square linear fitting, only those local maxima that were located within 10 min of the initial guesses were used. In this way, we avoided the necessity to sift through all maxima manually for each patch, setting instead only the start and end time for the patch. The local maxima that were selected for the fitting are shown by the dots with digits that indicate the patch number and the final regression lines are shown by the solid black lines. Note that the patch numbering scheme here is completely different from the one used in Fig. 1 (we have here 8 patches versus 19).

The absorption patch velocity estimates from the keograms are used later in Sect. 7 where we compare them with velocities obtained using the primary method used in this study described below. Panels (c) and (d) of Fig. 2 show the geographic latitude and longitude, respectively, of the absorption maximum location in the IRIS FoV versus time. The maximum positions were determined from the absorption images as discussed above (Fig. 1). The maxima for each individual patch are connected with the coloured lines; the colour of the line is the same as the colour of the half-power contour in Fig. 1 (with the substitution of the yellow lines by the red ones, more appropriate for the diagram colour scheme). To calculate the patch velocity we again fitted straight lines (least-square fit) to the absorption maximum positions for each patch, separately for x and y components. The linear regression coefficients for each patch are indicated in Figs. 2c–d by the red digits. One should note here that the drift velocity calculations are rather straightforward in this method; the drift velocity from the regression lines gives the "true" components of the absorption maximum velocity, while the drift velocity from the keograms gives only the apparent velocity that needs to be converted to the true patch velocity, as discussed later in Sect. 7.

The direction (azimuth from the geographic north through the geographic east) of the obtained patch drift velocity is shown in Fig. 2e by the coloured horizontal lines with the patch numbers indicated by the red digits. The thickness of the line corresponds to the quality of the fitting: the heavier the line, the higher the regression coefficient (minimum of the two coefficients for x and y components).

Also shown in Fig. 2e are ΔX and ΔY components of magnetic perturbations (heavy and light black lines, respectively) recorded by the KIL magnetometer. The quiet day curve was deduced from magnetometer records from the three quiet days in February 2001, indicated in the bottom part of Fig. 2e. Assuming that the magnetic perturbations were mainly caused by the convection-related Hall electrojet currents (Fukushima, 1976), the azimuth of the electrojet plasma flow (opposite to the current direction) was derived from the magnetometer data by rotating the direction of the horizontal magnetic perturbations by 270°. This azimuth is plotted in Fig. 2e by the blue line whose thickness corresponds to the total magnitude of magnetic horizontal perturbations $\Delta H = (\Delta X^2 + \Delta Y^2)^{1/2}$.

One can notice in Fig. 2e a reasonable agreement between the directions of the absorption patch drift and electrojet flow derived from the magnetic perturbations. These directions are at ∼90°, that is eastward during the first half of the period and at ∼−90° (westward) during the last 1.5 h with the variable values in between. The agreement is better for the patches of sufficiently long duration (e.g. patches 00, 02–08, 13, 15). The periods with not very good agreement (e.g.

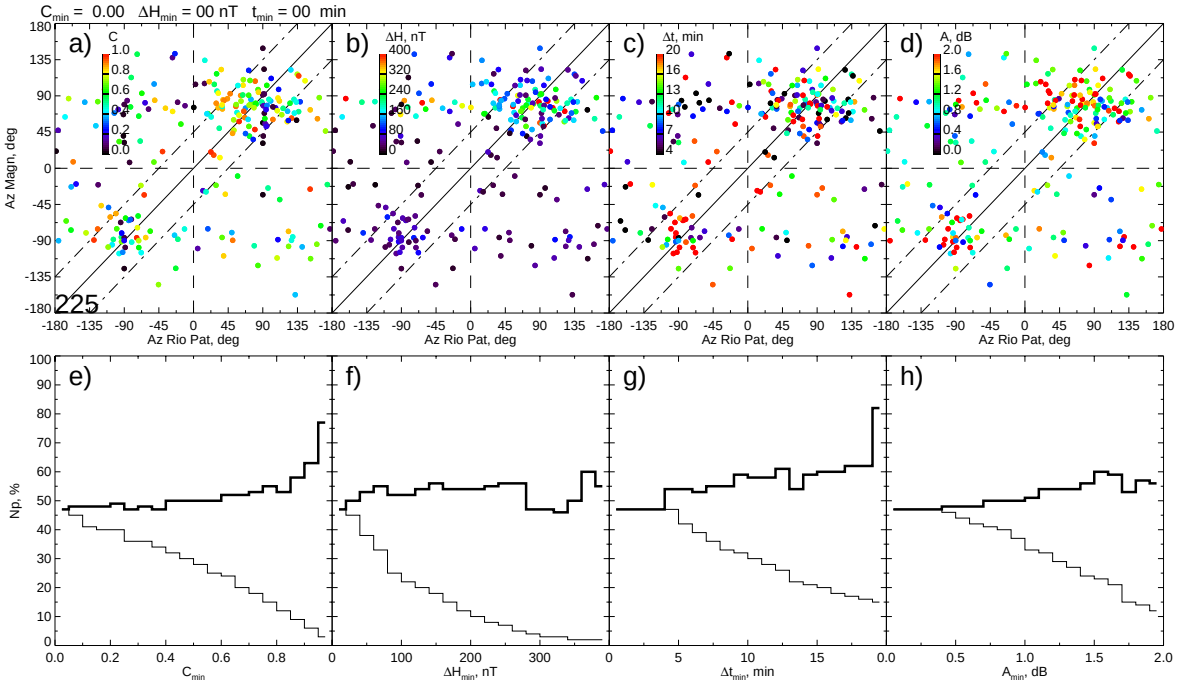

Fig. 3. Scatter plots of the azimuth of the electrojet plasma flow versus the azimuth of the absorption patch drift. Each dot is colour coded in **(a)** correlation coefficient C, **(b)** total magnitude of horizontal perturbations ΔH, **(c)** patch duration Δt, and **(d)** absorption intensity A. The colour code bar is shown in the top left corner of each panel. The total number of points is indicated in the bottom left corner of panel (a). Panels **(e)–(h)** show by a heavy black line the percentage of points above a certain threshold in parameter from a respective panel (a)–(d) that is located within 45° of the ideal coincidence line. The thin line shows the percentage of points within 45° and above a certain threshold with respect to the total number of points.

long-duration patches 09 and 11) are clearly associated with the changes in the flow direction polarity indicated in Fig. 2e by the vertical solid lines. In the next section we explore the relationship between the absorption drifts and electrojet flow using the data for all 10 events.

4 Absorption patch drifts and electrojet flow

In Fig. 3 we compare (point-by-point) the azimuth of the absorption patch drift with the average azimuth (for the patch duration) of electrojet flow for all considered events, Table 1. Altogether 225 absorption patches were identified using the method described in Sect. 3. To identify the parameter(s) that might affect the quality of the absorption patch velocity determination, all points in Fig. 3 are colour-coded in (a) correlation coefficient $C = \min(C_x, C_y)$, (b) the total magnitude of horizontal magnetic perturbations ΔH, (c) patch duration Δt, and (d) absorption intensity maximum A. As mentioned, Δt was limited by 20 min. The maximum values for ΔH and A were 850 nT and 5.3 dB, respectively, with the majority ($>\sim$90%) of points having $\Delta H < 400$ nT, $A < 2$ dB. In the correlation coefficient calculations we discarded one outsider point to eliminate the effects of the sudden jumps (by less than 100 km) in the CNA maximum location with successive return to the original position that most likely did not represent the actual motion but rather a sudden, short-lived (1–2 min) CNA intensification at some other location within the same patch, as, for example, at 04:46 UT in Figs. 1, 2c, 2d. One can see that, similar to the previous section, there is a general agreement between the azimuths; the majority of points are within 45° of the ideal coincidence line (we selected a ± 45° limit simply as a boundary between directions that are closer to the plasma drift direction and the ones that are closer to the perpendicular direction; these boundaries are shown by dash-dotted lines). Of the four parameters of interest, the points with greater C, Δt, and A tend to concentrate in the vicinity of the ideal coincidence line. To emphasize this point, we show in panels (e)–(h) with a heavy line the number of points above a certain threshold in the respective parameter with a relatively good agreement (±45° of the ideal coincidence) divided by the number of all points above the same threshold (in %). For reference we also show with a thin line the percentage of points with good agreement with respect to the total number (225). Thus, for example, from panel (e), 50% of points with the correlation coefficient C between 0.5 and 1.0 have good agreement, while in total the points with C =0.5–1.0 and good agreement constitute 25% of all 225 points. Clearly, the agreement improves with the increase in C, Δt, and A, while it does not change much with the ΔH increase. We also notice that the percentage of points with larger ΔH drops faster (thin line) than in any other histogram. Having that in mind, for further analysis we restricted the database of absorption patches by

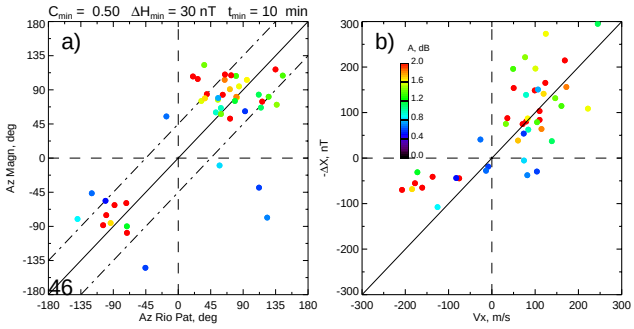

Fig. 4. Panel **(a)** The same as Fig. 3d but with additional criteria applied. Panel **(b)** shows the scatter plot of the magnetic perturbations $-\Delta X$ versus zonal velocity of patch motion V_x.

imposing the following criteria: C_{min}≡0.5, ΔH_{min}≡30 nT, and Δt_{min}≡10 min.

Figure 4a shows the points that satisfy these new criteria. In total, there are 46 absorption patches in the new database. One can immediately notice that the agreement is indeed much better. The analysis analogous to that of Figs. 3e–h shows that at least 70% of points are within 45° of the ideal coincidence line. The points with worst agreement tend to have smaller absorption maximum values. In panel (b) we show a similar scatter plot, the reversed north component of magnetic perturbations $-\Delta X$ versus zonal component of the patch drift velocity V_x. The sign of the magnetic perturbations is opposite to that of the zonal component of drift velocity (except for 4 points in the bottom-right and top-left quadrants). The points of the same sign are all located close to zero, both in terms of velocity and magnetic perturbations. The points with small absorption tend to have small velocities and magnetic perturbations. The zonal velocities are not high, with the typical values of the order of 150 m/s for both east- and westward drifts. Magnetic perturbations, on the other hand, tend to be smaller in amplitude for westward propagating patches than for eastward drifting ones (50 nT versus 50–200 nT).

One can conclude from Figs. 3, 4 that the absorption patches drift in the direction which is close to that of the electrojet plasma flow derived from magnetic perturbations. If so, the absorption patches should reverse their drift direction (from eastward to westward) at the same time as the electrojet flow does. In the example presented in Fig. 2 we saw that this was approximately the case; from the keogram, the absorption drift reversal was observed at 07:22 UT, close to the reversal in magnetic azimuth at 07:16 UT (vertical solid line in Fig. 2e). The analysis of the absorption patch motion based on the tracing of the absorption maximum in successive locations confirmed this result; patch 10 (∼07:00 UT) was drifting eastward, while patch 11 (∼07:15 UT) was drifting westward. To assess how well the reversals in the riometer and magnetometer data correspond to each other in all 10 events we performed the following analysis.

The absorption drift direction reversals $t_{rev\ keo}$ were identified from the keograms for all 10 events (two for event 2);

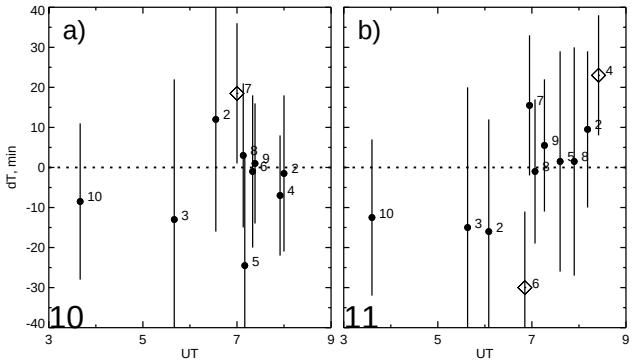

Fig. 5. The time difference between the motion direction reversals as determined from two different methods versus the reversal time from the second method: **(a)** from the absorption images and keograms and **(b)** from the absorption images and magnetic perturbations. The total number of points is indicated in the bottom left corner of each panel. The diamonds mark the points that are farther from the zero time difference than the estimate uncertainty (vertical bars). The digits by each point indicate the event number from Table 1.

these reversals are given in the last column of Table 1. The drift reversals were also determined from the analysis of the drift direction for successive absorption patches as described below. We first identified successive patches with zonal drifts in opposite directions and above a threshold of 20° in drift azimuth magnitude. Only the absorption patches of sufficiently long duration Δt_{min}=7 min and high correlation coefficient (the highest of the two) C_{min}=0.6 were considered here. The absorption patch drift reversal time was then set to the mean of the start time of the first patch t^1_{st} and the end time of the second patch t^2_{end}, $t_{rev\ pat}\equiv(t^1_{st}+t^2_{end})/2$. The uncertainty in reversal time in this method was set to $(t^2_{end}-t^1_{st})/2$. The reversal time estimates calculated in this method were shown in Fig. 2e by the dotted vertical lines with the uncertainties shown by the dashed vertical lines.

To check that the two methods of reversal time calculations (from the keograms and from the absorption images) give comparable results we plotted the time difference $t_{rev\ keo}-t_{rev\ pat}$ versus $t_{rev\ keo}$ in Fig. 5a. The uncertainty in $t_{rev\ keo}$ was assumed to be zero for the present purpose. Digits near each point indicate the event number from Table 1. There are 10 (out of 11 total) reversals $t_{rev\ keo}$ that have a corresponding reversal $t_{rev\ pat}$ within 30 min. The points are clustered evenly around the horizontal line of ideal coincidence and only one point (7, marked by the diamond) is farther from the zero line than the estimate uncertainty. In panel (b) we compare the reversal times from the magnetometer data $t_{rev\ magn}$ (shown by solid vertical lines in Fig. 2e) with the closest reversals $t_{rev\ pat}$ (dotted lines in Fig. 2e) by plotting the difference between those against $t_{rev\ magn}$. Again, with the exception of event 1 all reversals in the electrojet flow had corresponding reversals in absorption patch drift direction. Two reversals (both in magnetometer and riometer data) were identified for event 8, whereas only

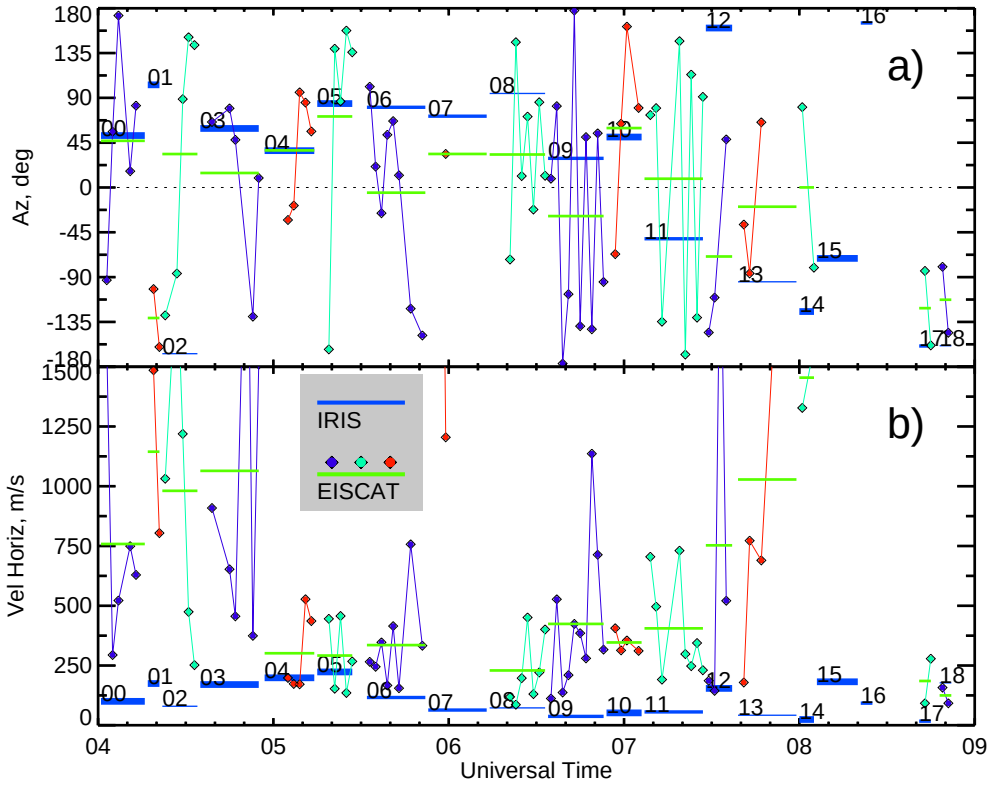

Fig. 6. Comparison of the IRIS absorption drift and EISCAT convection velocities in **(a)** azimuth and **(b)** magnitude. Blue lines show the absorption drifts with the digits indicating the patch number from Fig. 2e. Diamonds connected with the thin lines correspond to the EISCAT ion drift measurements at 2-min resolution simultaneous with the absorption patches from Figs. 1, 2e (the colour scheme is the same as in Fig. 2e). Green horizontal lines show the average EISCAT ion drift velocities (for the patch duration).

one such reversal was identified in keogram. The overall agreement is satisfactory, with only two points located farther from the zero line than the estimate uncertainty. A similar result was obtained by plotting $t_{rev\ magn} - t_{rev\ keo}$ versus $t_{rev\ keo}$ (not presented here). One can conclude that within the estimate uncertainty the reversals in the riometer absorption drift direction were almost coincident with the reversals in the electrojet flow direction derived from magnetic perturbations.

5 Ion drifts and ionospheric conductances from the EISCAT measurements

In the previous section we compared the absorption drift directions with those of the electrojet plasma flow derived from the magnetic perturbations under an assumption that the latter are mainly produced by the Hall ionospheric currents and showed that these directions were close to each other. A comparison of the absorption drifts and Doppler velocities measured by ionospheric radars such as CUTLASS (HF), STARE (VHF), and EISCAT (UHF) is another way of exploring the relationship between the absorption drift and plasma convection. Unfortunately, during none of the 10 events of interest the HF/VHF echo occurrence near the IRIS FoV was high enough to produce reliable convection velocity estimates. The EISCAT tristatic ion drift velocity measurements from which the plasma convection velocity in the F-region ($\boldsymbol{E}\times\boldsymbol{B}$ drift) can be inferred, were performed only during one event (14 February 2001) and in this section we present these data. One should note, however, that the quality of the EISCAT data during this event was not fully conducive for comparisons with the IRIS-inferred drifts, e.g. for the exact zonal drift reversal time determination, partly due to the technical problem with remote site computers (the transmitter power was not transmitted properly to the remote sites), resulting in minor measurement errors introduced during the data analysis for which a fixed value of the transmitter power had to be assumed.

In Fig. 6 we present the comparison between the IRIS and EISCAT horizontal velocities in (a) geographic azimuth and (b) magnitude for 14 February 2001, 04:00–09:00 UT. Blue lines represent the IRIS absorption patch drifts from Fig. 2e. The digits nearby show the patch number. Diamonds show the EISCAT horizontal velocities at 2-min resolution. The average EISCAT velocities (for the patch duration) are shown by green lines and the EISCAT data points used for this averaging (including points above the maximum velocity in panel (b)) are colour-coded according to the colour scheme of Fig. 2e. We have excluded all points with unrealistically high velocity $V_{EISCAT} > 5$ km/s.

The EISCAT convection velocity gradually changes its direction from eastward to westward, panel (a), although the scatter in the EISCAT data points is quite large (except for the last 30 min). The reversal occurs between 06:30 and 08:00 UT. The agreement between IRIS and EISCAT drift direction is quite good, especially for patches with higher correlation coefficients 00, 04, 05, and 10 (shown as in Fig. 2e by thicker lines). Unfortunately, there is no simultaneous EISCAT data for the critical, westward drifting patch 15. The only "good" patch for which the difference in azimuths is above 15° is patch 03. We would like to point out, however, that this large difference is almost entirely due to one blue point with negative azimuth of −135° at ∼04:52 UT. The agreement between velocity magnitudes is much worse, panel (b), with the IRIS drifts being significantly lower, though one can notice that the EISCAT drifts decrease towards the middle of the interval of interest (06:00 UT), where the IRIS drifts are minimized as well (patch 07) and that for the intervals with smaller point scatter the disagreement is smaller, too. The latter suggests that the relatively large disagreement between velocity magnitudes could be related to the rapid fluctuations in the electric field intensity that are not seen through the imaging riometer technique but detected by incoherent radar as occasional high-velocity measurements, which, on average, result in larger EISCAT velocity magnitudes.

Another issue that should be addressed in the context of the EISCAT data is the relationship between the absorption drift and ionospheric conductance. More specifically, we attempt to relate absorption to the height-integrated conductivity and to assess the role that the conductance gradients may play in the determination of the Hall current direction from equivalent currents. Indeed, even though inferring this direction from the magnetometer records is rather a standard technique (e.g. Stauning et al., 1995), its applicability may be questionable when, for example, the electron density/conductivity distribution in the ionosphere is not homogeneous as discussed below.

The height-integrated horizontal ionospheric current $\boldsymbol{J}$ is related to the Pedersen (Σ_P) and Hall (Σ_H) conductances and electric field through Ohm's law:

$$\boldsymbol{J} = \Sigma_P \boldsymbol{E} + \Sigma_H (\hat{\boldsymbol{b}} \times \boldsymbol{E}) , \quad (1)$$

where $\hat{\boldsymbol{b}} \equiv \boldsymbol{B}/B$ is assumed to point downwards. The curl of the toroidal (divergence-free) component of the current $\boldsymbol{J}_T$ identical with the equivalent current $\boldsymbol{J}_{eq}$ derived from magnetic perturbations is given by:

$$\nabla \times \boldsymbol{J}_T = \nabla \times (\Sigma_P \boldsymbol{E}) + \nabla \times (\Sigma_H \hat{\boldsymbol{b}} \times \boldsymbol{E}) \quad (2)$$

and can be approximated as:

$$\nabla \times \boldsymbol{J}_T \cong \nabla \Sigma_P \times \boldsymbol{E} + \nabla \Sigma_H \times (\hat{\boldsymbol{b}} \times \boldsymbol{E}) + \Sigma_H \hat{\boldsymbol{b}} \nabla \cdot \boldsymbol{E} . \quad (3)$$

To derive the real electrojet currents $\boldsymbol{J}$ from the magnetic perturbations one needs the information on the large-scale distribution of either ionospheric conductances (e.g. Kamide et al., 1981) or electric fields from which the former can be estimated (Inhester et al., 1992; Amm, 1995). Since the imaging riometer data from which the conductance gradients can be inferred, was available only near the KIL magnetometer site and since the electric field distribution (e.g. from coherent radars) information was not available, we are not in a position to accurately compute the real currents. In addition, global techniques applied to the local problems often lead to large uncertainties (Murison et al., 1985; Knipp et al., 1994). We can nevertheless estimate the effects of the conductance gradients on the errors associated with the assumption that the equivalent currents are equal to the Hall currents/conductance homogeneity. Thus, from Eq. (3), this error depends on the relative contribution of the first term as compared to the other two terms and hence on the ratios $\nabla \Sigma_P / \nabla \Sigma_H$ and $\nabla \Sigma_P / \Sigma_H$. Under the assumption of the fixed ratio $\alpha \equiv \Sigma_H / \Sigma_P$ at any point, it follows that $\nabla \Sigma_P / \nabla \Sigma_H = 1/\alpha$ and $\nabla \Sigma_P / \Sigma_H = 1/\alpha \nabla \Sigma_H / \Sigma_H$. Hence, we should consider the relative gradient $\nabla \Sigma_H / \Sigma_H$.

We next present the EISCAT data and ionospheric characteristics derived from these measurements and model parameters. Figure 7a shows the EISCAT electron density data from 84.4 to 173.5 km on 14 February 2001, 04:00–11:00 UT. The raw data from the Tromsø site have been analyzed with a 2-min resolution using the alternating coding scheme. The minimal altitude of 84.4 km was selected, since during the analysis it was found that the density data below the fully decoded altitude of 87.4 km (90-km range) exhibited regular changes that were consistent with the density measurements above 87.4 km in at least one 3-km gate. The EISCAT densities have been calibrated using the Tromsø Dynasonde data for the same period. The data points that had negative densities or temperatures (not shown) have been excluded from further analysis. Panels (b) and (c) show the Pedersen and Hall conductivities, respectively, estimated from the EISCAT densities, electron temperatures and model collision frequencies according to the standard formulas (e.g. Kelley, 1989, p. 39). The collision frequencies have been calculated by using the expressions given by Schunk and Walker (1973) and Schunk and Nagy (1978) and neutral atmosphere density profiles given by the MSISE-90 thermospheric model for the time (14 February 2001, 06:00 and 09:00 UT, for night- and daytime measurements, respectively) and location of measurements (IRIS FoV centre). The red dots in panels (b) and (c) are the height-integrated (84–173 km) Pedersen (Σ_P) and Hall (Σ_H) conductivities in arbitrary scale. These values have been assigned to a specific time only if the percentage of altitude ranges with density/temperature data was above 50%, so that the intervals when the EISCAT measurements were patchy (as, for example, near 08:00 UT) have been excluded. Finally, the yellow curves show the model height-integrated conductivities due to the sunlight (Robinson and Vondrak, 1984). The ratio between Hall and Pedersen conductances α, panel (d), was of the order of 3 for the entire period of interest. This ratio was slightly higher during the night.

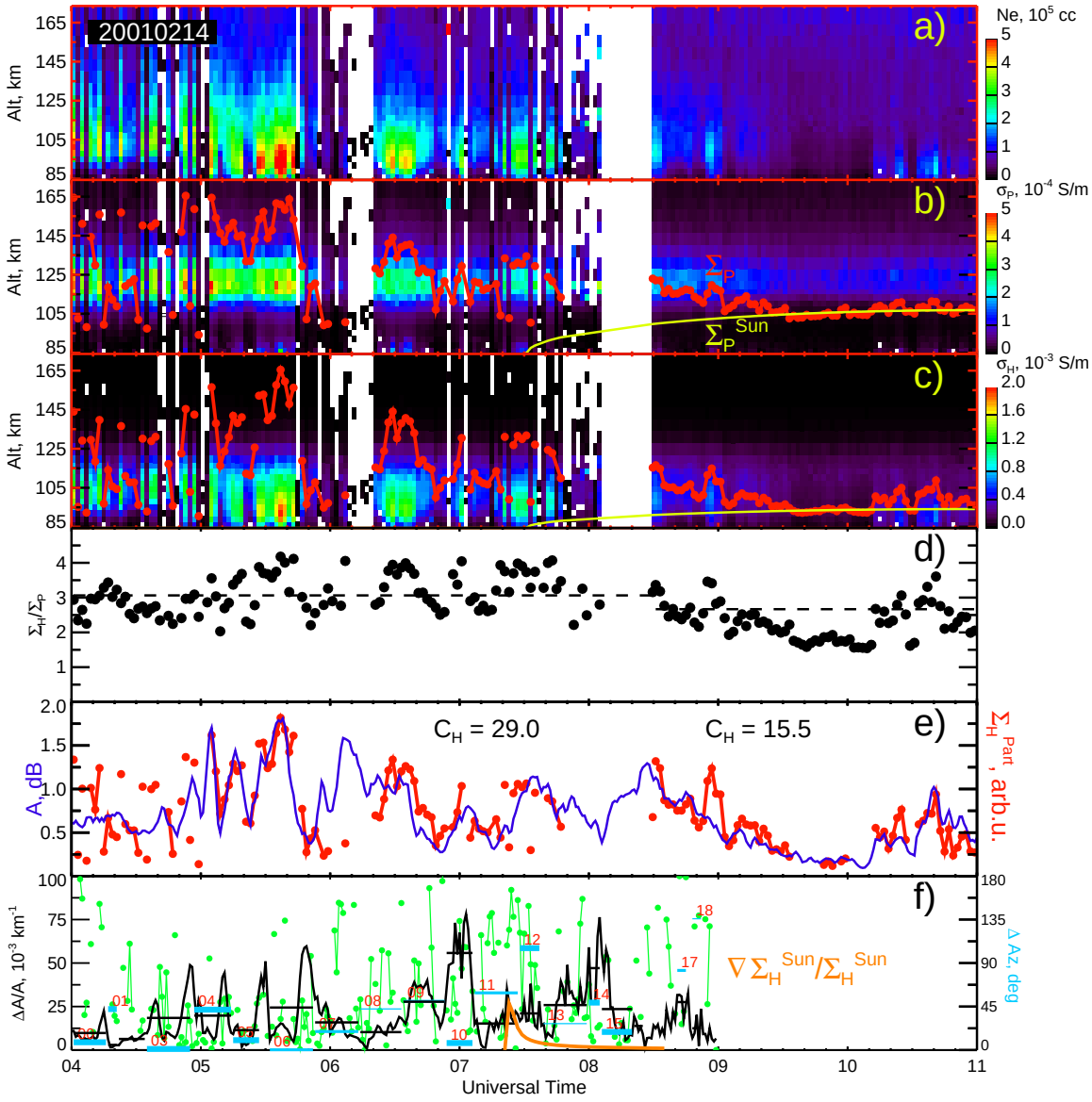

Fig. 7. Ionospheric conductances from the EISCAT measurements on 14 February 2001, 04:00–11:00 UT. First three panels show **(a)** the electron density N_e, **(b)** Pedersen conductivity σ_P, and **(c)** Hall conductivity σ_H from 84.4 to 173.5 km. The colour bars are shown on the right of each panel. Also shown in panels (b) and (c) by red dots and lines are the Pedersen (Σ_P) and Hall (Σ_H) conductances, respectively, and the model conductances (Σ_P^{Sun} and Σ_H^{Sun}) due to the sunlight (Robinson and Vondrak, 1984). Panel **(d)** shows the ratio $\alpha = \Sigma_H/\Sigma_P$ with the average night- and daytime ratios (3.06 and 2.66, respectively) shown by dashed lines. Panel **(e)** shows the absorption intensity at IRIS beam 16 (blue), together with the normalized Hall conductance due to the particle precipitation Σ_H^{Part} (red). The scaling coefficient $C_H = \Sigma_H^{Part}/A$ is different for night- and daytime conditions, as indicated on the top of panel (e). The red dots in panel (e) are connected only if the difference between neighbour points is less than 0.5 dB. The bottom panel **(f)** shows by a black line the relative gradient of absorption $\Delta A/A$ at the IRIS FoV centre (IRIS beam 25) and by blue lines the difference in drift azimuths ΔAz= |Az Magn −Az Rio| as determined from absorption images and magnetometer records from Fig. 2e. The relative gradient of the conductance due to the sunlight $\nabla\Sigma_H^{Sun}/\Sigma_H^{Sun}$ is shown by the orange line. The black horizontal lines indicate the average relative absorption gradients (for the patch duration). The instantaneous (1-min resolution) difference in azimuths is shown by green dots (connected if the difference between neighbour points <45°).

In panel (e) we show by blue line the absorption intensity measured in beam 16 of IRIS, the beam closest to that of EISCAT at 90 km. The Hall conductance due to the particle precipitation only, $\Sigma_H^{Part} \equiv \sqrt{\Sigma_H^2 - (\Sigma_H^{Sun})^2}$, is shown in panel (e) by red dots/lines in arbitrary scale. The scaling coefficients $C_H = \Sigma_H^{Part}/A$ were selected separately for the night- and daytime conditions. Some of the red dots are significantly lower than the blue line, but more detailed inspection reveals that these points in most of the cases refer

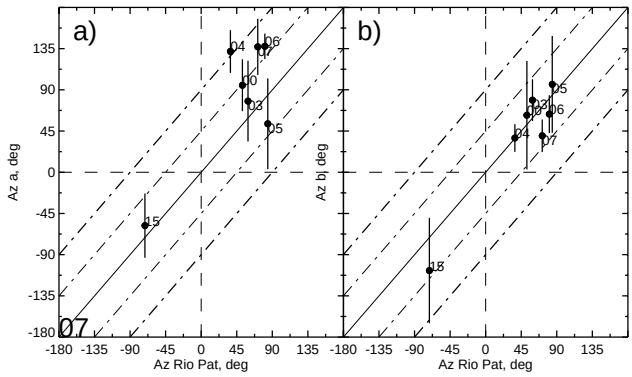

Fig. 8. The azimuth of the patch's **(a)** longest and **(b)** shortest dimension versus azimuth of the patch drift from 14 February 2001 for C_{min}=0.5, ΔH_{min}=30 nT, Δt_{min}=10 min. The digits by each point indicate the patch number, Figs. 1, 2e.

to those 2-min intervals during which density is greatly reduced as compared to the intervals immediately before and after, as, for example, at 07:22 and 07:32 UT. In general, however, absorption A is correlated quite well with the Hall conductance due to the particle precipitation Σ_H^{Part}.

Assuming that a similar relationship exists also for any other point within the IRIS FoV, the effects of the conductance gradients on the agreement between riometer- and magnetometer-inferred drift directions can be estimated. We have to remember, however, that consideration of the relative gradients is more appropriate, as discussed above. Figure 7f shows the comparison between the relative gradient in absorption intensity $\Delta A/A$ at the IRIS FoV centre and the difference between drift directions determined from riometer (Az Rio) and magnetometer (Az Magn) data. The relative gradient in conductance due to the sunlight $\nabla\Sigma_H^{Sun}/\Sigma_H^{Sun}$ is shown by the orange line. The average differences ΔAz≡|Az Rio–Az Magn| taken from Fig. 2e are shown by horizontal blue lines and the average relative absorption gradients (for the patch duration) are shown by black lines.

The relative gradients due to the sunlight $\nabla\Sigma_H^{Sun}/\Sigma_H^{Sun}$ are small, except for the interval immediately after the sunrise (07:22 UT) and even then they are smaller than the gradients associated with the particle precipitation $\Delta A/A \cong \nabla\Sigma_H^{Part}/\Sigma_H^{Part}$. The dependence $\frac{\nabla\Sigma_H}{\Sigma_H} = F(\frac{\nabla\Sigma_H^{Sun}}{\Sigma_H^{Sun}}, \frac{\nabla\Sigma_H^{Part}}{\Sigma_H^{Part}})$ is rather complex because of the nonlinear dependence of Σ_H upon Σ_H^{Sun} and Σ_H^{Part} but from Fig. 7f it can be approximated as $\nabla\Sigma_H/\Sigma_H \cong \nabla\Sigma_H^{Part}/\Sigma_H^{Part} \sim \Delta A/A$ for almost the entire period of interest. There is no clear relationship between the average ΔAz and $\Delta A/A$, e.g. patches 03 and 04 are associated with the comparable $\Delta A/A$ (black) but ΔAz (blue) is much larger for patch 04. One might think that a comparison of the average parameters is less meaningful in a situation when gradients at a fixed observational point exhibit high variability, while the absorption drifts are estimated from the tracing of the absorption patches in the entire FoV and that a similar comparison on a smaller time scale could be more appropriate. To achieve this we computed the "instantaneous" differences in azimuths in a manner similar to that described in Sect. 3, except that instead of considering the motion of the absorption intensity maximum for long intervals (10–20 min) we considered the motions for each 1 min of measurements. To reduce the data scatter inevitable in such a crude method of velocity determination we discarded all 1-min intervals during which the absorption maximum jumped by more than 25 km. We show these instantaneous differences by green dots, Fig. 7f. Despite the difference in approach, one still cannot recognize any clear relationship between gradients and the difference in azimuths, except for the interval 05:00–06:00 UT when the larger differences are associated with the larger gradients. Interestingly enough, this was also the interval during which the absorption was highly correlated with the Hall conductance, Fig. 7e.

6 Absorption patch drifts and orientation

In Fig. 1 we presented an example of the absorption intensity images that showed a large variability in the absorption patch shape, orientation, and drift velocity. In this section we further explore the relationship between the direction of absorption patch drift and those of the patch's longest and shortest dimensions (determined as described in Sect. 3). In Fig. 8a (8b) we have plotted the azimuth of the patch's longest (shortest) dimension, "Az a" ("Az b"), versus azimuth of the patch drift direction, "Az Rio Pat". As before, we limited the number of patches from 14 February 2001 using criteria C_{min}=0.5, ΔH_{min}=30 nT, Δt_{min}=10 min. The digits near each point in Fig. 8 indicate the patch number. Figure 8 also shows the standard deviations for azimuth of the longest and shortest dimensions.

In case of the elongated region with enhanced absorption propagating in the direction perpendicular to the direction of elongation one would expect that the azimuths of the absorption patch's longest dimension (Az a) would be located near the lines that denote perpendicularity with the patch drift direction (outer diagonal lines), while the azimuths of the shortest dimension (Az b) would be located close to the ideal coincidence line (solid diagonal line). Figure 8 confirms these expectations but only to a certain extent. Indeed, from Fig. 8b, the direction of the shortest dimension is very close to the drift direction. In Fig. 8a, however, quite a few points lie within ±45° lines, that is closer to the drift vector than to the perpendicular direction. The standard deviations for some points in both estimates, however, were quite large. To reduce uncertainties associated with these particular estimates, for the next diagram we restricted the database to encompass only the points with standard deviations less than 30°, Fig. 9. From the event on 14 February 2001 only points 04 and 06 have sufficiently small deviations, so that in this diagram we show the data from all events. In addition, to

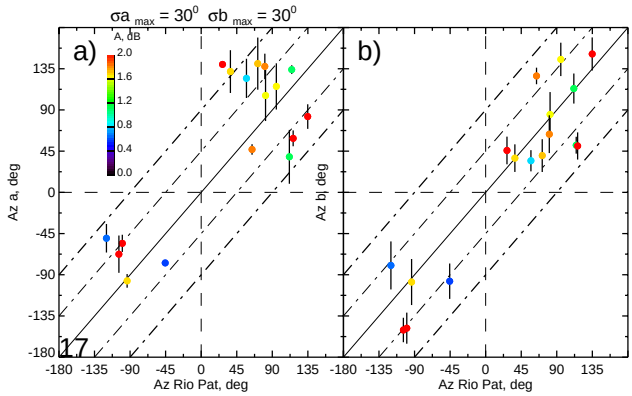

Fig. 9. The same as Fig. 8 but for all events and patches when the standard deviation in average azimuth (both for longest and shortest dimensions) was below 30°. The points are colour-coded in absorption intensity. The colour bar is shown in the top left corner of panel **(a)**.

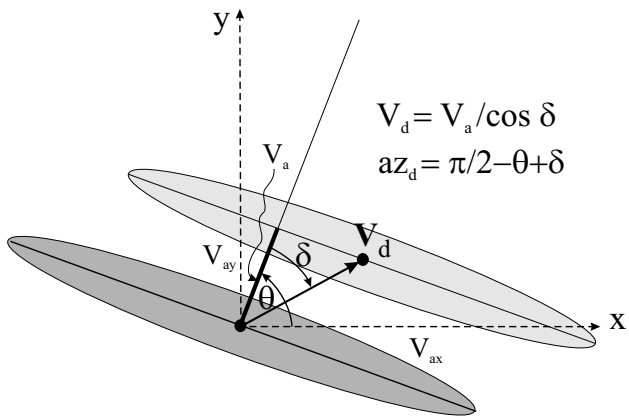

Fig. 10. Motion of elongated absorption patch. The initial (final) patch position is shown by the dark (light) ellipse. The velocity of apparent motion (perpendicular to the longest patch dimension) V_a is obtained from the apparent velocities along the axes V_{ax} and V_{ay}.

check whether the absorption intensity has any effect on the data in this presentation, all points in Fig. 9 are colour coded in absorption. Despite the limitations, the situation is quite similar to that of Fig. 8. The majority of points in Fig. 9b are located close to the ideal coincidence line, whereas there are at least 4 points in Fig. 9a with sufficiently small deviations to say for sure that they are also located close to the drift direction. Finally, there seems to be no consistent pattern in Fig. 9 with respect to the absorption intensity.

7 Absorption patch drifts from images and keograms

In Sect. 3 we described two methods of the absorption patch velocity calculations, the first method is based on the tracing of the absorption intensity maximum positions in the absorption "square-shaped" FoV images, deriving velocity components from the regression lines, and constructing the total drift velocity vector as a simple vectorial sum of components. An alternative way is to use the information from the single row and column of the riometer beams ("cross-shaped" FoV), which is the case, for example, for presentation in the form of absorption keograms. In this method, however, the construction of the total drift velocity vector is not so straightforward (see below) and in general requires making an assumption about the direction of the drift. More precisely, an arc-like absorption enhancement is often assumed to propagate perpendicular to the direction of elongation. The data presented in this report, on the other hand, suggest that this is not always the case (Figs. 1, 9a).

In Fig. 10 we illustrate the motion of an elongated patch and the patch velocity calculations, assuming an arbitrary patch drift direction with respect to the patch elongation. As the patch drifts from the initial position, shown by dark grey ellipse, to the final position (light grey ellipse), the successive narrow riometer beams along the x and y axes would record the passage of the absorption maximum through the beam, from the timing of which the apparent velocities V_{ax} and V_{ay}, respectively, can be deduced. Using these values and assuming a certain rotation of the drift velocity vector from the direction perpendicular to elongation (angle δ in Fig. 10) the total patch velocity can be constructed as follows:

$$\theta = \tan^{-1}\frac{V_{ax}}{V_{ay}}, \qquad V_a = V_{ax}\cos\theta\,, \tag{4}$$

$$\mathrm{az}_d = \frac{\pi}{2} - \theta + \delta, \quad V_d = V_a/\cos\delta\,, \tag{5}$$

where V_a and θ (V_d and az_d) are the magnitude and direction of the apparent (true) drift velocity vector. Note that the angle θ is counted from the x axis counterclockwise, while the drift azimuth az_d is counted from the y axis in the clockwise direction.

The second method (from the apparent motion in keograms) is limited in a sense that the angle δ has to be assumed, whereas the first method (from the absorption images) can provide both the total velocity vector $\boldsymbol{V}_d$ and the angle δ. It is, therefore, of particular interest to compare the drift velocities obtained using these two methods. Figures 11a–b show the result of such a comparison for (a) drift azimuths and (b) drift magnitudes from 14 February 2001, assuming $\delta\equiv 0$. The digits by each point indicate the patch number (in the numeration scheme of Figs. 1 and 2e). The drift velocity from the absorption keograms ("Az Rio Keo" and V_{keo}) was calculated for the closest (within 20 min) "keogram patch" to those "image patches" that satisfied the criteria of Fig. 4. Thus, patches 03–07, 15 (Figs. 1, 2e) are compared with patches 00–04, 07 in Figs. 2a–b. The overall agreement in Figs. 11a–b is satisfactory. The points 05 and 15 have the worst agreement, both in terms of azimuth and magnitude; for both patches the keogram method underestimates the drift velocity. The reason for this underestimation can be the finite rotation of the drift velocity vector away from the perpendicularity with the patch elongation. According to Eq. (5), the drift velocity increases with δ as $1/\cos\delta$,

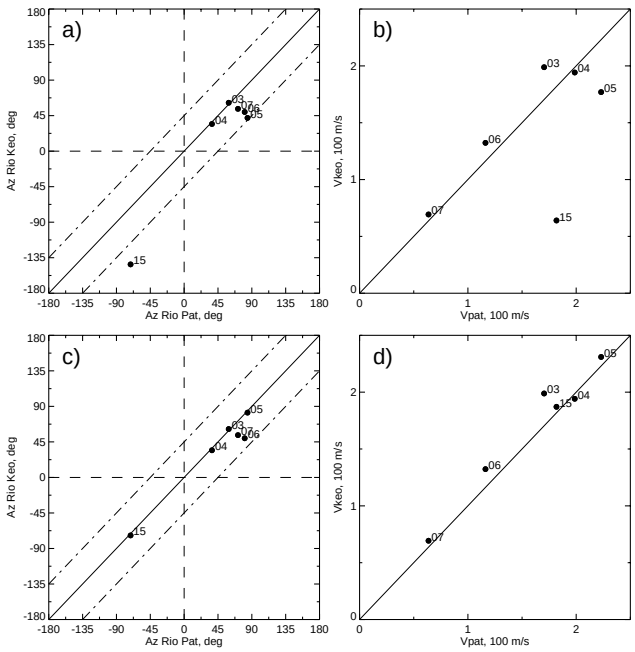

Fig. 11. Comparison of the **(a)** azimuths and **(b)** speeds of the patch drift motion on 14 February 2001 as determined from absorption keograms and images. The digits by each point indicate the patch number, Figs. 1, 2e. Panels **(c)** and **(d)** show the same comparison but with the assumed additional rotation of the velocity vector for points 05 and 15.

so that one can introduce a necessary correction for velocity simply by assuming some finite angle δ. Figures 11c–d show the same comparison as Figs. 11a–b, but with "correction" angles δ=40° and δ=70° for patches 05 and 15, respectively. One can see a significantly better agreement both in magnitude and azimuth of the drift velocity. The correction angles are in agreement with the data presented in Fig. 8a, in which the average deviations from perpendicularity were 58° and 77° for patches 05 and 15, respectively, with the uncertainties of ∼40°. Thus, using velocities of the patch apparent motion inferred from the keograms and by assuming that some patches were drifting in a direction that was different from perpendicularity to elongation, it is possible to reproduce the results obtained from the absorption images.

8 Summary and discussion

In this study we concentrated on the motions of the steadily drifting absorption structures in the morning sector. For the analysis we selected 10 events featuring the change in the zonal component of drift velocity from east- to westward.

In the past, zonally propagating absorption structures have been associated with the precipitating electrons injected into the nightside ionosphere at substorm expansion phase onset. The motion of electrons with energies in excess of 25 keV (required to produce a considerable absorption) is expected to be governed by the combined effect of the inhomogeneity and curvature of the geomagnetic field (GC drift) (Roederer, 1967, 1970). Experimentally, however, Berkey et al. (1974) demonstrated that, even though in most events the observed velocities of the absorption eastward expansion of 0.7–7 km/s were close to velocities expected for the 50–300 keV electrons, during some events the eastward expansion velocity was as high as 20 km/s, which would require unrealistically high energies if the GC drift interpretation was to be used.

In our observations, the absorption drifts were much slower, with the typical zonal velocities of the order of 150 m/s, Fig. 4b. For these velocities to be associated with the GC mechanism the precipitating electrons should be very soft (ε<10 keV) and hence very unlikely to cause a noticeable absorption on the ground. A similar result was obtained in the study by Hargreaves and Berry (1976), who reported the median absorption peak eastward speeds of 38 km/min (633 m/s). In an earlier study by Hargreaves (1970) the range of reported speeds was wider (from 80 m/s to 3.3 km/s), but for pre-midnight observations the drift direction was predominantly westward, in sharp contrast with the gradient-curvature hypothesis which implies eastward drifts for all time sectors. The great variability in velocity in Hargreaves (1970) suggested that the absorption structures move with the $\boldsymbol{E}\times\boldsymbol{B}$ rather than with the gradient-curvature drift. Later, Kikuchi and Yamagishi (1990) and Kikuchi et al. (1990) presented evidence that the drift pattern of the small-scale (30–60 km in width) absorption structures was essentially the same as the drift pattern derived by Hargreaves (1970) using riometers separated by ∼250 km. Kikuchi et al. (1990) also noticed a similarity between the absorption drift pattern and that of magnetospheric convection, although the data statistics was relatively low (13 drift events). In this context the absorption drift observations in various time sectors become of crucial importance. Kainuma et al. (2001) considered 106 absorption drift events between 13:00 and 07:00 MLT and found a reasonable agreement between their results and those of Hargreaves (1970) and Kikuchi et al. (1990).

In the present study we considered a comparable number of drift events (225 events without restrictions and 46 with restrictions, Sect. 4) in the morning sector (06:00–12:00 MLT) the observations from which were poorly represented in the previous studies. The auroral absorption drift observations from these magnetic local times are also important, since one can expect the ionospheric convection to be reversed near magnetic noon, so that one can check whether the sense of absorption drift is reversed, too. Following this idea, instead of plotting the drift velocities for each individual drift event versus MLT in a statistical fashion similar to previous studies (Hargreaves, 1970; Kikuchi et al., 1990; Kainuma et al., 2001), we considered a series of drift events, thus monitoring the absorption motions continuously, which allowed us to identify the reversal times. We would like to note here that the present report appears to be the first example of continuous observations of absorption drifts that showed a clear change in the sense of zonal motions.

Furthermore, we compared the reversal times derived from the absorption data with those of the electrojet plasma flow obtained from the magnetic perturbations and found a reasonable agreement, Fig. 5b. Another important observation is that the drift directions of the individual absorption patches agree well with those of the electrojet plasma flow, Fig. 4a. These two results were in agreement with the results of comparison between absorption patch drift and EISCAT plasma convection velocities based on the limited data set, Fig. 6. All of the above leads us to conclude that the absorption structures in our observations were drifting with the velocities consistent with the $\boldsymbol{E}\times\boldsymbol{B}$ drift mechanism.

This result disagrees with those of Nielsen (1980) and del Pozo et al. (2002), who presented several examples demonstrating a significant difference between the absorption and $\boldsymbol{E}\times\boldsymbol{B}$ drift velocities, but one has to keep in mind that their observations were performed near magnetic midnight during the substorm expansion phase, while ours refer to a different MLT sector, for which the $\boldsymbol{E}\times\boldsymbol{B}$ drift mechanism seems to be dominating (Kavanagh et al., 2002).

The question remains, however, why the precipitating electrons that have sufficiently high energy ($\varepsilon>25$ keV) to be detected by riometers on the ground, drift with much slower velocity than the one implied by the trapped particle theory. Kikuchi et al. (1990) suggested that the hot plasma cloud injected into the region of closed field lines from the magnetotail at the substorm onset propagates with the GC drift until it encounters another plasma cloud populated with colder particles. This results in the pitch-angle scattering of the high-energy electrons into the loss cone with the successive precipitation at the D-region altitudes. In this scenario, even though the precipitating electrons still have sufficiently high energy to cause considerable absorption, the region where the actual precipitation occurs is essentially an ionospheric projection of the "intersection" between hot and cold plasma clouds and hence its motion is controlled by that of the slower, cold particles.

A condition for the electrons to propagate with the velocity close to that of the $\boldsymbol{E}\times\boldsymbol{B}$ drift can be readily obtained from the expression for the electron drift velocity (e.g. Roederer, 1970):

$$\boldsymbol{V}_D = \frac{E}{B}\boldsymbol{i} + \frac{\varepsilon}{BR_c}(1+\cos^2\alpha)\boldsymbol{j}, \tag{6}$$

where $\boldsymbol{i}$ and $\boldsymbol{j}$ are the unit vectors directed along the $\boldsymbol{E}\times\boldsymbol{B}$ and GC drift directions, respectively, ε is the energy in eV, R_c is the magnetic field line radius of curvature, and α is the pitch angle. For a dipolar field, $R_c=LR_E/3$, where R_E is the Earth's radius, and hence the ratio between the second (GC) and the first ($\boldsymbol{E}\times\boldsymbol{B}$) term magnitudes in Eq. (6) is $3(1+\cos^2\alpha)/(LR_E)\varepsilon/E$. For electrons with $\alpha=0$ at $L=6$ this becomes $\sim 1/6\varepsilon/E$ if ε and E are expressed in keV and mV/m, respectively. For a radial magnetospheric electric field $E_{\mathrm{RM}}=1$ mV/m, resulting in a meridional ionospheric electric field $E_{\mathrm{MI}}=2L(L-3/4)^{1/2}E_{\mathrm{RM}}$ (Mozer, 1970) of 27.5 mV/m, this implies $\varepsilon<6$ keV for the $\boldsymbol{E}\times\boldsymbol{B}$ drift to dominate over the GC drift.

In this interpretation the drift velocity is determined by the electric field. The low drift velocity magnitudes reported in this study are then almost for certain related to the fact that the observations were performed near the zonal flow reversals, where velocity is close to zero. Unlike the drift velocities, the magnetic perturbations associated with the absorption enhancements were not symmetric with respect to the drift reversal. Thus, we noticed in Fig. 4b a certain asymmetry between the magnitudes of ΔX for positive and negative ΔX corresponding to the westward and eastward plasma flows, respectively. Interestingly, a similar feature can be recognized in the data presented by Kikuchi et al. (1990) (see their Fig. 7), although with faster zonal velocities observed (from -500 to $+800$ m/s). The fact that in Fig. 4b the points with the lowest V_x and ΔX had the smallest absorption intensity can be interpreted as follows. While V_x is a measure of the electric field, the auroral absorption is related to the ionospheric plasma density. The magnetic perturbations, in turn, are the measure of the electrojet current, which is the function of both electric field and conductivity/plasma density. In the case when both electric field and density are small the magnetic perturbations are expected to be small, too, consistent with the data presented in Fig. 4b.

The problem with this interpretation is that an increase in the ionospheric conductivity associated with the enhanced absorption typically occurs at D-region altitudes around 90 km, which is somewhat lower than the typical electrojet height of 110 km. With the electron energy decrease, however, the height where most of the ionization takes place increases (e.g. Rees, 1964), and although it is generally true that the corresponding absorption decreases drastically, the absorption events of low intensity (say, below 0.5 dB) could be related to the plasma density increase at 95–100 km altitudes. Rocket measurements showed that the height of absorption maximum at night can be from 90 to 95 km with the half-power width of absorption peak of the order of 20 km (see, for example, a comprehensive review by Hargreaves, 1969, and references therein). Certainly, the issue about the height of absorption maximum is far from being resolved. With the construction of two new imaging riometers in Andøya (IRIS-AND) and Ramfjordmoen (ARIES) in Norway located close to the IRIS FoV it will be possible to determine the altitude of the principle absorption layer more precisely. The results of a similar experiment in Antarctica based on the simple vertical parallax technique showed that $\sim$50% of all (low- and high-intensity) CNA events are peaked above 90 km, with the median peak at 92.5 km (Terkildsen et al., 2004). How this altitude varies for different levels of CNA remains to be seen.

The EISCAT density data presented in Fig. 7a for an event on 14 February 2001 support the idea that the absorption enhancements were produced by the particles precipitating somewhat above the nominal absorption altitude of 90 km. The density was maximized at around 105 km in the beginning of the period of interest, 04:00–05:00 UT and at $\sim$95 km later, at around 05:30, 06:30, and 07:30 UT. This observation can partially explain the large discrepancies between

the EISCAT convection and IRIS drift velocity magnitudes simply because in the IRIS drift velocity calculations we assumed a height of 90 km. The correction (ratio of maximum height to 90 km) is larger in the beginning of the period, in agreement with the data presented in Fig. 6b, in which the ratio between EISCAT and IRIS velocity magnitudes was larger for this interval as well (04:00–05:00 UT). If one assumes a height of 105 km, as suggested by the EISCAT density data for this interval, the correction is $\sim 105/90 \cong 1.17$, which is still considerably less than the correction required to match the EISCAT- and IRIS-inferred drift magnitudes. The rapid fluctuations in the electric field intensity not detectable through the imaging riometer technique discussed in Sect. 5 could be the cause for the remaining part of the discrepancies. Another potential reason are the effects of the electric field spatial microstructure which are more pronounced for the smaller viewing area of the EISCAT radar. A similar conclusion has been reached by Davies et al. (1999), who reported greater EISCAT velocities as compared to those measured by the CUTLASS HF radar.

An alternative view is that significant discrepancies between the EISCAT- and IRIS-inferred drifts stem from the fact that the absorption patches do drift with the velocity, which is significantly different from that of the ambient plasma. Such examples have been presented in the past for the case of dynamic structures during the substorm conditions observed with riometers (Nielsen, 1980; del Pozo et al., 2002), as well as with optical instruments and magnetometers (e.g. Lühr et al., 1998). The limited amount of the plasma flow speed measurements available for comparison with absorption drift estimates of sufficient quality (high regression coefficients and long duration) prevents us from making a more definite conclusion as to whether absorption drifts are systematically lower than the $\boldsymbol{E}\times\boldsymbol{B}$ drift in velocity magnitude in the vicinity of the morning zonal drift reversals. Our results, showing reasonable agreement between absorption drift and plasma flow directions, on the other hand, support the $\boldsymbol{E}\times\boldsymbol{B}$ mechanism idea. Further comparisons between the absorption drift estimates from IRIS and plasma flow measurements from such facilities as EISCAT and CUTLASS in other time sectors should help resolve the issue. Another point requiring further investigation is the identification of the mechanism(s) associated with the absorption patches drifting with a velocity distinctly different from that of the ambient plasma.

The EISCAT density and electron temperature data on 14 February 2001 (together with the MSISE-90 neutral densities) have also been employed to compute the Pedersen and Hall conductances, Figs. 7b, c. The latter has been shown to correlate well with the absorption intensity in beam 16 of IRIS, the beam closest to that of EISCAT, which allowed us to estimate the effect of the conductance gradients on the difference between the electrojet flow direction (opposite to equivalent current) and that of the IRIS-inferred drifts. We found that the correlation between those two parameters was rather poor, Fig. 7f. In addition, the analysis similar to that performed in Fig. 3 for $\Delta A/A$ as a parameter showed almost no dependence of the difference between azimuths from the relative absorption gradients. One should bear in mind, however, that in our analysis we considered the relative gradient magnitudes and that a more sophisticated approach which would take into account additional parameter(s), such as relative orientation of the gradient and electric field (the information on which was not available in this study), might reveal the desired effect.

Another important result of this study is on the relationship between the absorption drift direction and the direction of the patch elongation. We demonstrated that, although most patches drifted in a direction close to perpendicularity with elongation, in agreement with the previous findings by Kikuchi et al. (1990) and Kainuma et al. (2001), a considerable number of patches in our observations drifted in a direction that was closer to that of elongation, Figs. 8, 9. We also compared the drift velocities obtained using the primary method adopted for this study, the tracing of the absorption intensity maximum locations in the absorption FoV images, with those obtained in a second, more traditional method, that is from the absorption keogram, and found overall agreement. For the absorption patches for which the agreement was the worst we introduced an additional rotation of the drift direction (which has to be assumed in the second method) away from the perpendicularity, with the patch elongation consistent with the estimates from Fig. 8 and showed a substantial improvement in agreement between the two methods, Fig. 11.

In this study we developed a simple method for absorption patch identification based on the tracing of the absorption intensity maximum positions inside the IRIS FoV, which, combined with the half-power contour information, provides a useful tool for studying fine features in the particle precipitation. Although we restricted the maximum number of frames for each patch (mainly to increase the reliability of the velocity estimates), thus artificially "multiplying" the number of patches, the application of the same procedure in the absence of such a limitation allows one to identify the absorption patches quite uniquely, so that instead of patches 07–10 in Fig. 1 there will be just one patch corresponding to patch 04 in Figs. 2a–b. The method does not require vast computational resources, nor does it involve excessive manual sifting through the data. In this method though the same patch reentering the FoV after the drift reversal would be classified as a separate patch since the IRIS FoV is relatively small ($\sim 200\times 200\,\mathrm{km}^2$), which makes it difficult to verify whether the reentering patch is indeed the same (e.g. by using the information on patch size/shape). Ideally, one would want to trace the absorption patches in much larger areas of the ionosphere, i.e. comparable to the all-sky-camera FoV ($\sim$1000 km in diameter). The new imaging riometers under construction, IRIS-AND and ARIES, should rectify this situation, enabling the restoration of the particle precipitation picture on a larger scale without compromising the good spatial resolution.

9 Conclusion

The first continuous observations of the drifting structures in auroral absorption in the morning sector near the zonal drift reversals presented in this report showed that the regions with enhanced absorption were drifting in a direction that was close to that of the electrojet plasma flow derived from horizontal magnetic perturbations and (for one event) tristatic ion drift velocities in the F-region. The drifting structures changed the direction of their motion from eastward to westward at approximately the same time as the plasma convection. Based on our results on the absorption drift direction, we consider the $\boldsymbol{E}\times\boldsymbol{B}$ drift to be the primary mechanism that determines the absorption drift velocity in the auroral zone in the morning sector, although more studies are needed to determine whether the absorption drift velocity magnitude is consistent with this mechanism. The present work based on the continuous observations of the absorption motions thus extends conclusions drawn from the previous observations of individual absorption drift events to the crucial region in the vicinity of the zonal drift reversals.

In this study we performed comparisons between the directions of the absorption drift with those of the absorption patch elongation obtained from the absorption intensity 7×7-beam images. These confirmed a general validity of the assumption about their perpendicularity, but also demonstrated a substantial deviation of the drift direction away from the perpendicularity with elongation in a number of cases, resulting in an underestimation of the patch velocity derived by tracing the absorption maximum in the single row-column of the riometer beams (e.g. from the absorption keograms). Our results suggest that the variability in the absorption patch shape, elongation, and drift direction is significantly larger than it was previously thought to be.

Acknowledgements. This research was supported by the Particle Physics and Astronomy Research Council, UK. The IRIS riometer is operated by the Department of Communication Systems at Lancaster University and funded by PPARC in collaboration with the Sodankylä Geophysical Observatory. The IMAGE magnetometer data are collected as a Finnish-German-Norwegian-Polish-Russian-Swedish project conducted by the Technical University of Braunschweig and Finnish Meteorological Institute. EISCAT is an International Association supported by Finland (SA), France (CNRS), Germany (MPG), Japan (NIPR), Norway (NFR), Sweden (NFR), and the UK (PPARC). We are grateful to N. F. Ness of BRI and CDAWeb for the ACE magnetic field data. We would like to thank A. Senior, A. Kavanagh, J. Hargreaves, H. Yamagishi and M. Pinnock for useful discussions and suggestions.

Topical Editor M. Lester thanks H. Lühr and E. Woodfield for their help in evaluating this paper.

References

Amm, O.: Direct determination of the local ionospheric Hall conductance distribution from two-dimensional electric and magnetic field data: Application of the method using models of typical ionospheric electrodynamic situations, J. Geophys. Res., 100, 21 473–21 488, 1995.

Berkey, F. T., Driatskiy, V. M., Henriksen, K., Hultqvist, B., Jelly, D. H., Shchuka, T. I., Theander, A., and Yliniemi, J.: A synoptic investigation of particle precipitation dynamics for 60 substorms in IQSY (1964–1965) and IASY (1969), Planet. Space Sci., 22, 255–307, 1974.

Browne, S., Hargreaves, J. K., and Honary, B.: An imaging riometer for ionospheric studies, Electronics and Communication, 7, 209–217, 1995.

Davies, J. A., Lester, M., Milan, S. E., and Yeoman, T. K.: A comparison of velocity measurements from the CUTLASS Finland radar and the EISCAT UHF system, Ann. Geophys., 17, 892–902, 1999.

del Pozo, C. F., Hargreaves, J. K., and Aylward, A. D.: Ion composition and effective ion recombination rate in the nighttime auroral lower ionosphere, J. Atmos. Sol. Terr. Phys., 59, 1919–1943, 1997.

del Pozo, C. F., Williams, P. J. S., Gazey, N. J., Smith, P. N., Honary, F., and Kosch, M. J.: Multi-instrument observations of the dynamics of auroral arcs: a case study, J. Atmos. Sol. Terr. Phys., 64, 1601–1616, 2002.

Detrick, D. L. and Rosenberg, T. J.: A phased-array radiowave imager for studies of cosmic noise absorption, Radio Sci., 25, 325–338, 1990.

Fukushima, N.: Generalized theorem for no ground magnetic effect of vertical currents connected with Pedersen currents in the uniform-conductivity ionsophere, Rep. Ionos. Space Res. Jpn., 30, 35–40, 1976.

Hargreaves, J. K.: Auroral absorption of HF radio waves in the ionosphere: A review of results from the first decade of riometry, Proc. IEEE, 57, 1348–1373, 1969.

Hargreaves, J. K.: Conjugate and closely-spaced observations of auroral radio absorption IV, Earth. Planet. Space, 18, 1691–1705, 1970.

Hargreaves, J. K. and Berry, M. G.: The eastward movement of the structure of auroral radio absorption events in the morning sector, Ann. Geophys., 32, 401–406, 1976.

Inhester, B., Untiedt, J., Segatz, M., and Kurschner, M.: Direct determination of the local ionospheric Hall conductance distribution from two-dimensional electric and magnetic field data, J. Geophys. Res., 97, 4073–4083, 1992.

Kainuma, S., Ishii, M., Murayama, Y., Kikuchi, T., Mori, H., and Igarashi, K.: Drift motion of ionospheric arc-like absorption regions observed with a 256-beam imaging riometer in Alaska, Earth. Planet. Space, 53, 753–760, 2001.

Kamide, Y., Matsushita, S., and Richmond, A. D.: Estimation of ionospheric electric fields, ionospheric currents, and field-aligned currents from ground magnetic records, J. Geophys. Res., 86, 801–813, 1981.

Kavanagh, A. J., Honary, F., McCrea, I. W., Donovan, E., Woodfield, E. E., Manninen, J., and Anderson, P. C.: Substorm related changes in precipitation in the dayside auroral zone – a multi instrument case study, Ann. Geophys., 20, 1321–1334, 2002.

Kelley, M. C.: The Earth's Ionosphere, Academic Press, San Diego, 1989.

Kikuchi, T. and Yamagishi, H.: Drift of auroral absorption observed with a scanning beam riometer at Syowa station, J. Comm. Res. Lab., 37, 1–14, 1990.

Kikuchi, T., Yamagishi, H., and Lester, M.: Drift of auroral absorption due to the magnetospheric convection observed with the scanning narrow beam riometer during SUNDIAL-86, Ann. Geophys., 8, 431–440, 1990.

Knipp, D. J., Emery, B. A., and Lu, G.: Application of the assimilative mapping of ionospheric electrodynamics (AMIE) procedure to cusp identification, in: Physical signatures of magnetospheric boundary layer processes, edited by Holtet, J. A. and Egeland, A., Kluwer Academic Publishers, 401–420, 1994.

Lühr, H., Aylward, A., Buchert, S. C., Pajunpaa, A., Pajunpaa, K., Holmboe, T., and Zalewski, S. M.: Westward moving dynamic substorm features observed with the IMAGE magnetometer network and other ground-based instruments, Ann. Geophys., 16, 425–440, 1998.

Mozer, F. S.: Electric field mapping from the ionosphere to the equatorial plane, Planet. Space Sci., 18, 259–263, 1970.

Murison, M., Richmond, A. D., and Matsushita, S.: Estimation of ionospheric electric fields and currents from a regional magnetometer array, J. Geophys. Res., 90, 3525–3530, 1985.

Nielsen, E.: Dynamics and spatial scale of auroral absorption spikes associated with the substorm expansion phase, J. Geophys. Res., 85, 2092–2098, 1980.

Nielsen, E. and Honary, F.: Observations of ionospheric flows and particle precipitation following a sudden commencement, Ann. Geophys., 18, 908–917, 2000.

Rees, M. H.: Note on the penetration of energetic electrons into the earth's atmosphere, Planet. Space Sci., 12, 722–725, 1964.

Rishbeth, H. and Williams, P. J. S.: The EISCAT ionospheric radar: The system and its early results, Q. J. R. Astron. Soc., 26, 478–512, 1985.

Robinson, R. M. and Vondrak, R. R.: Measurements of E region ionization and conductivity produced by solar illumination at high latitudes, J. Geophys. Res., 89, 3951–3956, 1984.

Roederer, J. G.: On the adiabatic motion of energetic particles in a model magnetosphere, J. Geophys. Res., 72, 981–992, 1967.

Roederer, J. G.: Dynamics of geomagnetically trapped radiation, Springer Verlag, New York, 1970.

Schunk, R. W. and Nagy, A. F.: Electron temperatures in the F-region of the ionosphere: Theory and observations, Rev. Geophys. Space Phys., 16, 355–399, 1978.

Schunk, R. W. and Walker, J. C. G.: Theoretical ion densities in the lower ionosphere, Planet. Space Sci., 21, 1875–1896, 1973.

Smith, C. W., Acuña, M. H., Burlaga, L. F., L'Heureux, J., Ness, N. F., and Scheifele, J.: The ACE magnetic field experiment, Space Sci. Rev., 86, 613–632, 1998.

Stauning, P., Clauer, C. R., Rosenberg, T. J., Friis-Christensen, E., and Sitar, R.: Observations of solar-wind-driven progression of interplanetary magnetic field B_Y-related dayside ionospheric disturbances, J. Geophys. Res., 100, 7567–7586, 1995.

Terkildsen, M. B., Fraser, B. J., and Yamagishi, H.: Determination of the altitudinal peak of cosmic noise absorption using a vertical parallax technique, Geophys. Res. Lett., 31, doi:10.1029/2003GL019068, 2004.